J. Fluid Mech. (2002), *vol.* 471, *pp.* 219–238. © 2002 Cambridge University Press
DOI: 10.1017/S0022112002002057 Printed in the United Kingdom

Fluid–structure interactions of a torsion spring pendulum at large initial amplitudes

By H. DÜTSCH, F. DURST AND A. MELLING

Institute of Fluid Mechanics, University of Erlangen–Nuremberg,
Cauerstrasse 4, D–91058 Erlangen, Germany

(Received 3 July 1999 and in revised form 20 May 2002)

The motion of a lamina of high aspect ratio suspended in a Newtonian fluid was studied experimentally and numerically. The damped oscillations for one rotational degree of freedom showed strong nonlinear fluid–structure interactions, mainly caused by the vortex structures forming at the lamina tips. The numerical results were obtained by a fully implicit Navier–Stokes solver, using partitioned coupling of the equations of motion of the fluid and suspended structure. Computations were carried out for different grid levels and time steps, providing information on the accuracy of the numerical results. For the fluid domain, a Langrangian–Eulerian finite-volume method was applied in order to solve the two-dimensional Navier–Stokes equation on grids moving with the oscillating lamina. The elastic motion of the lamina was computed as that of a torsion spring pendulum. The computed time traces of the angular position are in close agreement with corresponding experimental results. An equivalent empirical model which accounted for the fluid moments by empirical coefficients was much less successful in predicting the experimentally observed behaviour.

1. Introduction

Great advances in computational methods for the fluid and structure mechanics domains have been achieved in recent decades. Hence, the prediction of coupled mechanical phenomena, for large amplitudes in particular, is attracting increased interest in research and applications. The partitioned modular coupling of different solution methods has proved to be the most appropriate approach to obtain best results in each domain. To provide solutions for nonlinear multi-physical problems, efficient and robust coupling strategies have to be developed and investigated. This need motivated us to design a strongly coupled time-dependent configuration in order to investigate and to validate the computational predictions of dynamic interactions between fluids and structures at large displacements. For this purpose, the fluid-damped oscillation of a lamina was chosen. This involves the coupling between a torsion spring pendulum and a continuous viscous fluid flow, see figure 1, and has similarities to a check valve configuration as found in various civil engineering applications, see e.g. Horsten, van Steenhoven & van Campen (1990), Kerh & Wellford (1997). Designed as a single-degree-of-freedom oscillator it enabled very accurate modelling of the structural moments even at large amplitudes. Additionally, the high aspect ratio of the structure provided a two-dimensional flow pattern over a flow field large with respect to the lamina itself. As there was no mean cross-flow present in this configuration the structure interacted strongly with the self-induced fluid flow. Experiments were performed to determine the damping behaviour in air

https://doi.org/10.1017/S0022112002002057 Published online by Cambridge University Press

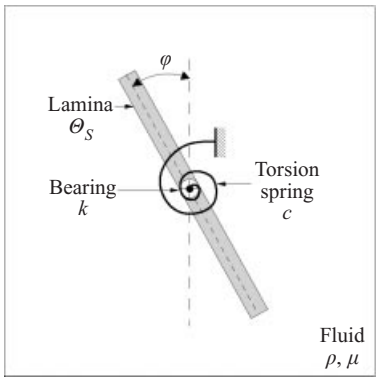


FIGURE 1. Fluid-damped torsion spring pendulum.

and water for initial excursions of 10°, 45° and −90°. Stationary measurements of the elastic properties of the torsion spring provided input data for the computational approach. Then the complementary numerical simulations allowed new insights into the coupled fluid and structure physics, i.e. the strong structure–vortex and vortex–vortex interaction phenomena.

The present paper describes experimental and numerical studies of the fluid–structure interaction and the results obtained. The main features of the test rig for the experimental investigations are described in § 2. In § 3 the mathematical treatment of the fluid–structure interaction is outlined for both the fluid and structure domains. The numerical method used to solve the resultant set of equations is briefly discussed and an alternative empirical model is also introduced. The experimental and numerical results are compared and discussed in § 4. Important conclusions of the work with respect to the characteristics of the flow field, the interaction with the motion of the structure and the suitability of the modelling adopted are presented in § 5.

The authors would be pleased to provide the experimental data for the purpose of validation and for bench marking on request.

2. Test-rig design and experimental set-up

The main objective of the experiment design was a two-dimensional rotational flow induced by the large-scale motion of a stiff structure. The design had to ensure that moments related to the structure domain could be determined very accurately in order to reduce error sources for the comparisons with the computations; an aspect ratio of 20 was, therefore, chosen for the lamina. End plates were mounted, in addition, to suppress the three-dimensionality of vortices, at least in the vicinity of the oscillating structure. Finally, the structural damping, e.g. the friction of bearings, was kept very low by mounting the lamina on a torsionless fibre. These features of the test-rig are presented in figure 2.

In detail the set-up consisted of a 1000 mm long sharp-edged lamina made from aluminium with a cross-section of 3.0 mm × 50.1 mm, immersed upright in the centre of a closed fluid tank with dimensions of 350 mm × 350 mm × 1100 mm. The lamina was arranged to oscillate around its longest axis of symmetry and in its relaxed position, i.e. 0°, was aligned parallel to the fluid tank walls. At the top and the bottom of the lamina 1.5 mm thick circular discs of 90 mm diameter were fixed at a distance of about 50 mm from the endwalls of the tank. Axles, which were arranged in slide

https://doi.org/10.1017/S0022112002002057 Published online by Cambridge University Press

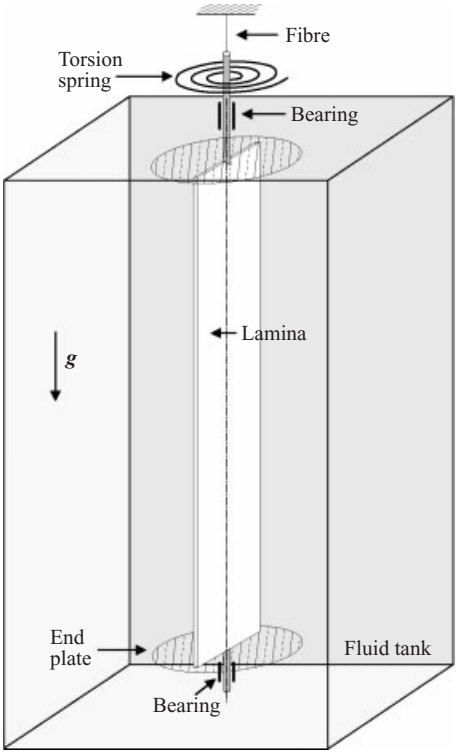


FIGURE 2. Main features of the test-rig design.

bearings made from Teflon, prohibited sideward motion of the lamina. The lamina was driven by a torsion spring and the complete oscillating structure was suspended from a torsionless fibre, which reduced the friction losses in the bearings significantly. It took about 140 cycles in air, for example, until the oscillator came to rest after an initial excursion of 45°.

It was not possible experimentally to follow the full time history of the damped motion of the structure from a single sequence of oscillations. Rather, from each of a large number of oscillation sequences with the same starting deflection a single data pair (angular position, time) was determined. Data pairs acquired over the whole duration of the motion were then combined to yield the temporal variation of angular position. For each test the angular ('stop') position of interest was prescribed relative to the rest position (where the spring force was zero). The lamina was deflected manually to the desired initial angle of excursion and allowed to start oscillating under the force of the torsional spring. The elapsed time between 'start' and 'stop' signals until the lamina reached the prescribed angle was then measured.

The start and stop signals were generated by two black plastic flags of very light construction which interrupted light beams aligned with the initial angle of excursion and the 'stop' angle respectively. Trigger pulses from two photodetectors then respectively activated and deactivated an electronic counter (Ballantine, model 5500B).

Although in principle a single flag interrupting the two light beams in turn would have sufficed, it was found that with this arrangement the 'stop' beam obstructed the 'start' beam for certain angles, or vice versa. Splitting the detection of the start and

https://doi.org/10.1017/S0022112002002057 Published online by Cambridge University Press

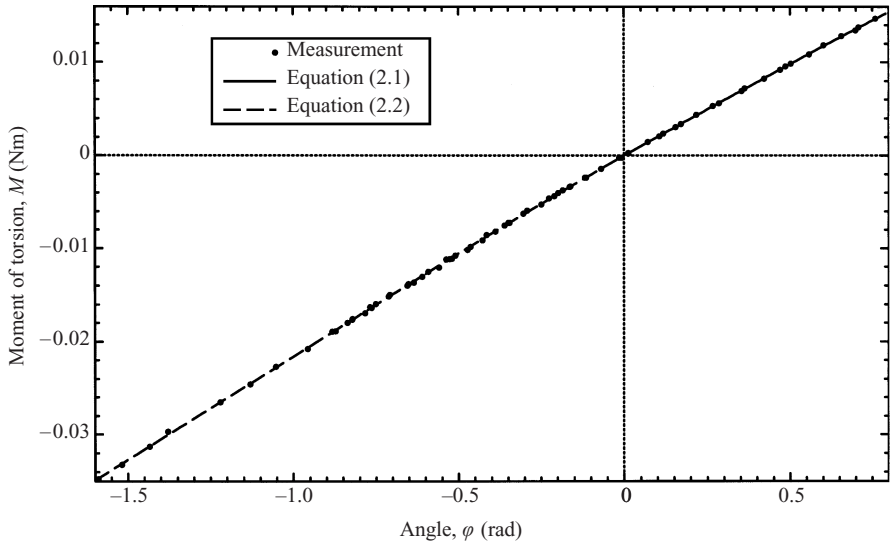


FIGURE 3. Measured spring characteristic and corresponding higher-order polynomials.

the stop signals with separate flag/beam pairs provided the advantage of permitting time measurements very close to the maximum positions regardless of the widths of the flags and the barriers. When tracking the oscillatory motion beyond the first cycle, multiple stop signals, of course, occurred. An electronic module, therefore, was implemented to skip a preset number of stop signals.

The positioning of each light barrier was determined within $\pm 0.1^\circ$. For a single swept angle at least three time measurements were performed in order to check the repeatability (better than 8 ms, i.e. about 1% of the period, in water and less than ± 2 ms in air). Between each single measurement at least 15 s relaxation time was allowed for the fluid in the tank to become still, so ensuring the reproducibility of the results.

For the start signal an angular offset between the start flag and the start light barrier (set by micrometer positioning) had to be accounted for. The initial time delay was kept less than 20 ms in all experiments. Details of the corresponding time correction are presented at the end of this section.

The oscillating structure was driven by a compression spring mounted on the top axle outside the fluid. This spring was modified to act purely in torsion. As the shape of the spring varied only a little even at large amplitudes, the inertial moment of the spring itself remained constant. This would have been difficult to achieve by a standard flat coil. The characteristic of the spring, see figure 3, was measured by loading it gravimetrically and fitting to a third-order polynomial by applying the method of least squares. Due to slight differences of the spring attachment two different regression functions

$$M = 2.0056 \times 10^{-2}\,\varphi - 8.4264 \times 10^{-4}\,\varphi^2 - 1.2525 \times 10^{-4}\,\varphi^3 \quad \text{for } \varphi > 0, \qquad (2.1)$$

$$M = 2.0419 \times 10^{-2}\,\varphi - 1.7001 \times 10^{-3}\,\varphi^2 - 5.1331 \times 10^{-4}\,\varphi^3 \quad \text{for } \varphi \leqslant 0 \qquad (2.2)$$

resulted for the positive and the negative angles, where the moment M is given in Nm and the angular position φ in rad. Corresponding to these equations the spring rate c was defined by two functions of φ, for the positive and the negative angles respectively. It was included in all computational models as $c(\varphi) = c_{sgn(\varphi)}(\varphi)$

https://doi.org/10.1017/S0022112002002057 Published online by Cambridge University Press

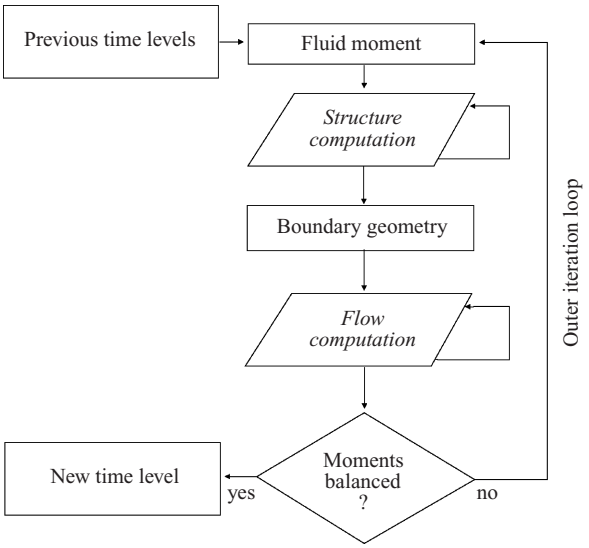


FIGURE 4. Partitioning scheme for the solution of coupled fluid–structure dynamics.

according to

$$M = c_+(\varphi)\,\varphi, \quad \text{if} \quad \varphi > 0, \tag{2.3}$$

$$M = c_-(\varphi)\,\varphi, \quad \text{if} \quad \varphi \leqslant 0. \tag{2.4}$$

For the evaluation of the results as well as for the numerical modelling, the structural damping was assumed to be related to the angular velocity $\dot{\varphi}$. From the experiments in air the structural damping coefficient k_S was then determined to be approximately $1.25 \times 10^{-5}\,\mathrm{rad^{-1}\,kg\,m^2\,s^{-1}}$, which was very low due to the fibre suspension. The corresponding damping ratio $k_S(4c\Theta_S)^{-1/2}$ was about 0.0036. Here, Θ_S denotes the inertial moment of the complete oscillating structure, which was calculated as $\Theta_S = 1.4992 \times 10^{-4}\,\mathrm{rad^{-1}\,kg\,m^2}$. Although this ratio was significantly less than 1, the structural damping moment was taken into account in all computations.

As previously mentioned, a constant delay angle was involved in the start time detection. Due to the micrometer positioning this angle could be determined accurately, but the corresponding time delay could not. Hence, this small time offset was computed from the parameter model presented in § 3.4. The equation of vibration of the structure was solved numerically taking into account the effects of the fluid flow by using a virtual inertia and a drag term. For each series of measurements the time offset was calculated and the measured time traces were corrected respectively.

3. Mathematical models and numerical methods

3.1. *Partitioned coupling*

When considering the physical domains it became obvious that the fluid flow and the structure vibration could not be solved independently. The two domains were coupled along their common boundaries. The structure dynamics depended on the forces and moments induced by the flow. The fluid dynamics was coupled to the kinematic and kinetic variables along the structure walls. In order to de-couple the physical models and to solve them in a partitioned approach an iterative procedure was applied which is sketched in figure 4. At each time level the conservation equations for the

https://doi.org/10.1017/S0022112002002057 Published online by Cambridge University Press

structure and the fluid domain were solved alternately. Therefore, the intermediate boundary conditions, i.e. the integral fluid moment as well as the position and the velocity of the lamina, were updated and exchanged between the domain models. The convergence was checked by the identity of the boundary conditions, the balance of the structural moments and the residuals of the flow solver, which provided an implicit-implicit scheme. Although the partitioned algorithms themselves were stable, this straightforward coupling proved to be unstable: full updating of the newest boundary conditions led to a rapid excitation that prohibited balanced consistent results. A geometric under-relaxation was, therefore, introduced to damp the outer iteration loop. Only part of the rate of change of the lamina position, as predicted from the structure computation, was passed to the flow computation. This treatment was also applied to minimize the number of outer iteration loops. Typically about one loop was necessary to decrease the normalized difference between the structure and the fluid moments by one order of magnitude. The alternative under-relaxation of the fluid moment gave a worse performance of the iterative process. More details of this approach and the numerical treatment have been presented in Dütsch, Melling & Durst (1999).

3.2. *Structure domain*

The structure dynamics was set up as a torsion-spring pendulum and, hence, modelled by the well-known equation of vibration

$$\Theta_S \ddot{\varphi} + k_S \dot{\varphi} + c(\varphi)\varphi = M_F(t) \tag{3.1}$$

with the angular position $\varphi(t)$ as the single degree of freedom dependent on the time t. This balance of moments was completed by the general coupling term M_F on the right-hand side that included all effects of the fluid domain.

Equation (3.1) was discretized by first-order-accurate implicit finite-difference schemes. For the first time derivative the Euler implicit scheme and for the second derivative the central difference scheme were chosen, and a constant time step was applied. By solving this equation in combination with the flow prediction a lamina position, which provided consistent boundary conditions for both physical domains, was determined at each time level.

For the efficient computation of a new time step it was very important to choose a good initial value for $M_F(t)$. Here, linear extrapolation proved to be a very good approach, when applying the converged fluid moments $M_F(t-\Delta t)$ and $M_F(t-2\Delta t)$ of the previous time levels. When starting the iterative process with the flow prediction and an estimated angle, even extrapolated, the partitioned scheme performed worse.

3.3. *Fluid domain*

For the prediction of the coupled fluid–structure behaviour the time-dependent load of the fluid acting on the structure had to be determined. This information was evaluated at discrete time levels from the numerical solution of the two-dimensional viscous flow in the cross-plane of the lamina. As the fluid motion was induced by the oscillating lamina the computation was performed on arbitrarily moving nodes using a Lagrangian–Eulerian formulation of the conservation equations. The corresponding integral form for a general transported scalar variable Φ is then

$$\frac{\mathrm{d}}{\mathrm{d}t}\iiint_V \rho\Phi \,\mathrm{d}V + \iint_S [\rho(\boldsymbol{v}-\boldsymbol{v}_g)\Phi - \Gamma_\Phi \,\mathrm{grad}\,\Phi]\boldsymbol{n}\,\mathrm{d}S = \iiint_V s_\Phi \,\mathrm{d}V, \tag{3.2}$$

https://doi.org/10.1017/S0022112002002057 Published online by Cambridge University Press

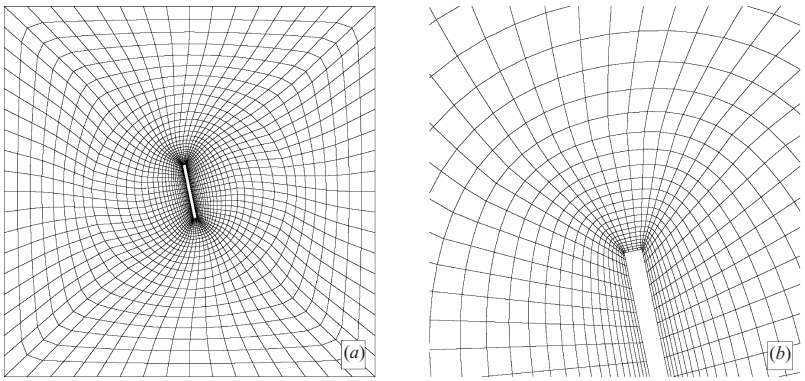


FIGURE 5. (*a*) Computational grid at a coarse refinement level (2176 cv), shown enlarged in (*b*).

where ρ represents the fluid density, $\boldsymbol{v}$ the Eulerian fluid velocity vector and $\boldsymbol{v}_g$ the corresponding grid velocity vector. Furthermore Γ_Φ is the diffusivity and s_Φ the volumetric source of the quantity Φ. V and S denote volume and surface respectively. In the present computations constant fluid properties were assumed for water ($\rho = 998.2\,\mathrm{kg\,m^{-3}}$, dynamic viscosity $\mu = 1.008 \times 10^{-3}\,\mathrm{Pa\,s}$) and for air ($\rho = 1.209\,\mathrm{kg\,m^{-3}}$, $\mu = 17.99 \times 10^{-6}\,\mathrm{Pa\,s}$).

The incompressible and laminar flow of a Newtonian fluid was solved on an O-type block-structured grid that was fitted exactly to the intermediate structure boundaries, see figure 5(*a*, *b*) for a coarse grid level. A finite-volume approach was applied for a SIMPLE-like algorithm, which was modified to deal with an arbitrary moving grid. The corresponding fundamentals are presented e.g. by Patankar (1980), Demirdžić & Perić (1990) and Durst *et al.* (1993).

In the present work a new, conservative discretization of the time derivative for a scalar Φ in equation (3.2) on a control volume V was applied in which the old control volume V^o is deformed to a new control volume V^n within a time step Δt:

$$\frac{\mathrm{d}}{\mathrm{d}t}\iiint_V \rho\Phi\,\mathrm{d}V \approx (\rho\Phi)^n\frac{V^n - V^o}{\Delta t} + V^n\frac{(\rho\Phi)^n - (\rho\Phi)^0}{\Delta t}. \tag{3.3}$$

The governing equations were solved in an inertial Cartesian reference system and the rotation of the lamina boundary was approximated by piecewise translational motion of the grid cells according to the Euler implicit time scheme. For a constant vector field in an infinite computational domain the flow can be treated as a solid body rotation. As the volume of each cell is then constant, the discretization problem discussed in Dütsch *et al.* (1999) is irrelevant with the conservative approach of Demirdžić & Perić (1990). The local rotation of each cell is taken into account by calculating the cell face vectors according to their orientation at each time level, so allowing consideration of both rotational and advective effects. The precision of the numerical result is limited by the kinematic approximation of the lamina rotation, i.e. by the time resolution. Nevertheless, consideration of a complementary term due to the local rotation of the coordinate system was unnecessary in this work, although it might be crucial in other applications.

The total fluid domain boundary was treated by a Dirichlet formulation, i.e. by providing velocity vector information. Hence, when considering the structure connected boundaries their angular positions and velocities were necessary as the input for the flow prediction. The computed pressure and shear force distributions

https://doi.org/10.1017/S0022112002002057 Published online by Cambridge University Press

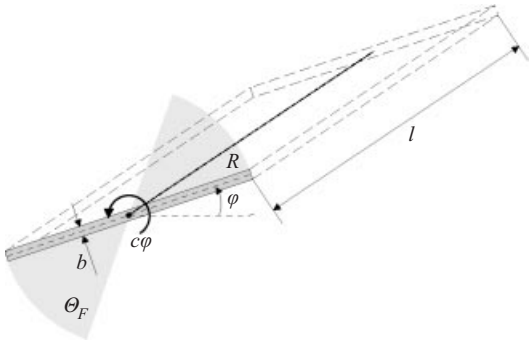


FIGURE 6. Visualization of the virtual moment of inertia.

along the common boundary were then evaluated to obtain the moment reaction of the fluid flow. Computations were performed on four different grid levels, starting from 34 control volumes (cv) along the lamina circumference (544 cv in total) up to 272 cv (34 816 cv in total).

To visualize the flow dynamics the distribution of the vorticity Ω was computed. It was defined as a cell-area-weighted mean value $\overline{\Omega}$ according to the relationship

$$\overline{\Omega} = \frac{1}{S}\int \Omega \,\mathrm{d}S = \frac{1}{S}\left(\oint u_1 \,\mathrm{d}x_1 + \oint u_2 \,\mathrm{d}x_2\right), \tag{3.4}$$

which was solved numerically.

3.4. *Empirical fluid model*

As an alternative approach to the coupled numerical simulation, a parameter model was applied in the present work. This model had its origin in an empirical theory which is widely used in engineering applications to describe the effects of fluid mass and fluid drag acting on a moving structure. For a translational motion path a constant virtual mass is added to the structure mass. Additionally, a constant drag coefficient c_d is assumed to model the nonlinear damping forces of the fluid flow. This added-mass theory is applied – to mention only one example – in the design of oscillating cylindrical structures in cross-flow, see e.g. Morison *et al.* (1950) or Lin, Bearman & Graham (1996). This theory could be applied to a rotational motion, when introducing a virtual inertia added to the moment of inertia of the structure alone. The right-hand side of equation (3.1) is then

$$M_F = -\Theta_F \ddot{\varphi} - k_F \dot{\varphi}|\dot{\varphi}|. \tag{3.5}$$

The virtual inertia Θ_F can be expressed more clearly by defining a virtual inertia coefficient c_i according to the relationship

$$\Theta_F = c_i \tfrac{1}{2}\pi\rho l R^4. \tag{3.6}$$

Here, R denotes the half-width of the lamina and l its length, see figure 6. One could consider $\frac{1}{2}\pi\rho l R^4$ as the moment of inertia of a circular cylinder filled with fluid that is swept by the full rotational motion of the lamina. The virtual inertia coefficient c_i, then, accounts for that volume fraction which has to be accelerated in addition to the structure, see figure 6.

The damping coefficient k_F can be determined from a drag coefficient formulation such as given by

$$k_F = c_d \tfrac{2}{3}\rho l R^4. \tag{3.7}$$

https://doi.org/10.1017/S0022112002002057 Published online by Cambridge University Press

The tangential velocity $R\dot{\varphi}$ at the tip of the lamina was chosen to define the dynamic pressure and $\frac{2}{3}R$ was chosen as a characteristic length scale to obtain the fluid drag moment.

Both terms in (3.5) were discretized consistently to the left-hand side of (3.1). Finally, this nonlinear model was solved numerically with at least 10 000 time steps per period.

In this parameter model pairs of coefficients, c_i and c_d, were determined by best fits to the present experimental results. However, a detailed comparison with the measured data permitted a check on the validity of the model terms, for large amplitudes in particular.

As the right-hand side of (3.5) approximated the total fluid flow behaviour, the solution of this model permitted the verification of the partitioned approach according to figure 4. This treatment provided a very valuable economical tool to study in advance the stability and convergence of the partitioned numerical method.

4. Results and discussion

4.1. *Oscillatory behaviour in air*

Since the dynamic processes of strong nonlinear fluid–structure coupling were of interest, initial amplitudes φ_0 of 10°, 45° and −90° were chosen to investigate the interaction mechanisms in a dense fluid by a complementary experimental and numerical approach.

The pendulum configuration was characterized by a natural period of 541.1 ms at low excursions, i.e. for almost linear behaviour. At amplitudes of about 45° a period of 539.4 ms for the first cycles was evaluated from numerical solutions of (3.1) for $M_F = 0$. The measurements in air (45.20°) then revealed a characteristic period of 539.6 ms close to the beginning of the motion and an average of 542.3 ms for the total oscillation time.

The predictions of the damping behaviour in air by both the partitioned computations and the empirical model were in close agreement with the experimental results. From the empirical model, the parameters $c_d = 2.8 \pm 0.4$ and $c_i = 0.31 \pm 0.01$ were determined to fit the time trace within the accuracy of the measurements. For both prediction models a time step of at most 0.1 ms had to be applied in order to prevent significant numerical damping.

In figure 7 a time sequence of the computed vorticity field is presented. The continuous curves denote positive contours of the vorticity with anticlockwise orientation and the broken curves negative contours, i.e. clockwise orientation. Large eddies induced by the lamina motion formed a complex arrangement of vortices and free shear layers. The oscillations of the structure, however, were hardly influenced by the fluid flow at all. In fact, the system behaviour was characterized more closely by forced mixing flow than by significant fluid–structure interactions. As a result of this weak coupling, the outer iterations of the partitioned approach needed no artificial stabilization, e.g. by under-relaxation.

Generally, the flow pattern and fluid loading developed perfectly symmetrically with the point of rotation in all investigated cases. In the text to follow, therefore, the presentation of the findings concentrates on only one side of the lamina.

4.2. *Oscillatory behaviour in water*

When the structure was surrounded with the dense fluid water, the oscillation of the lamina changed drastically compared with air, indicating significant coupling between

https://doi.org/10.1017/S0022112002002057 Published online by Cambridge University Press



FIGURE 7. Vorticity isolines for $\varphi_0 = 45°$ (air).

the structure and the fluid. Generally, the presence of the liquid reduced the natural frequency and increased the damping of the structure. The period for 10°, for example, increased to 811.3 ms. Moreover, the vortices generated behaved as the memory of the fluid motion, leading to extraordinary damping effects for higher initial excursions.

The time traces of the lamina oscillation are presented in figures 8, 9 and 10 for initial angles of 10.08°, 45.15° and −89.70°. The experimental data points are marked with error bars for both the angular position and the measured time, see also § 2. The uncertainty in the time measurement ($\leqslant 8$ ms), however, was so small that the error bars effectively disappear on the scale of these graphs. On increasing the initial excursion the attenuation of the amplitude became more pronounced in the first few cycles. In the case of −89.70° the oscillation collapsed almost totally after the first cycle. An oscillation with amplitudes of a few degrees remained, however, and since this was damped much less than at the beginning, it took about 16 cycles until the lamina stopped moving.

This damping behaviour was compared with the partitioned computational results on different grid levels and for different time steps. To obtain information as accurate as that from the experiments a time resolution of at least 1 ms was required. For a large initial excursion the requirements were even higher, although the period did

https://doi.org/10.1017/S0022112002002057 Published online by Cambridge University Press

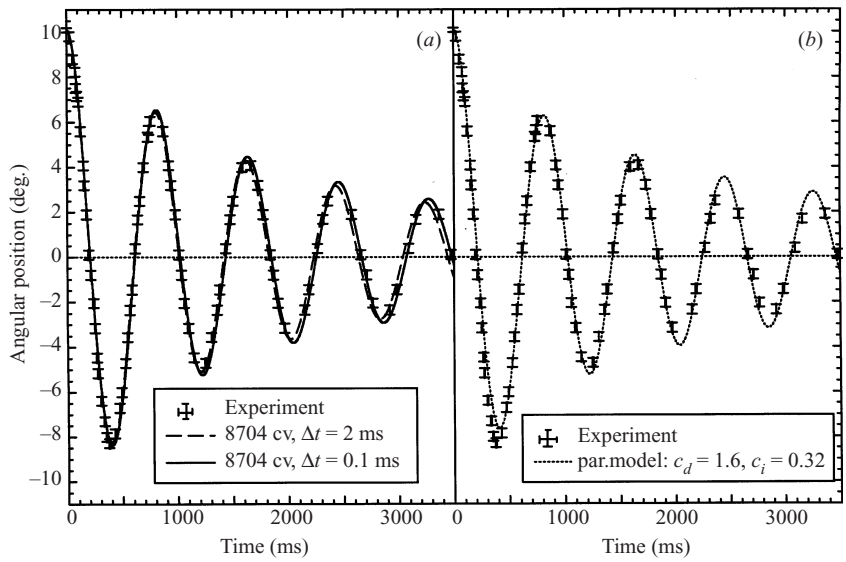


FIGURE 8. Comparison of the computed damping behaviour (*a*) and of the parameter model (*b*) with measurements for 10° initial excursion.

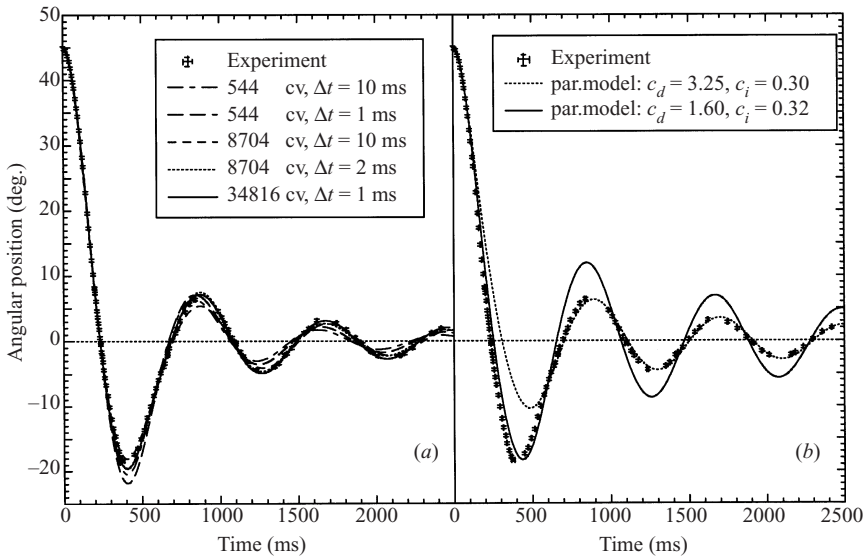


FIGURE 9. Comparison of the computed damping behaviour for different grid levels and time steps at 45° initial angle (*a*). Results of the parameter model (*b*).

not change significantly. Generally, a grid resolution of 8704 cv provided acceptable results.

4.2.1. *Empirical model*

In order to apply the alternative model of virtual inertia the parameters c_i and c_d had to be determined first. For an initial excursion of 10.08° the parameters $c_i = 0.32$ and $c_d = 1.60$ were found to be optimal, because they predicted the measured

https://doi.org/10.1017/S0022112002002057 Published online by Cambridge University Press

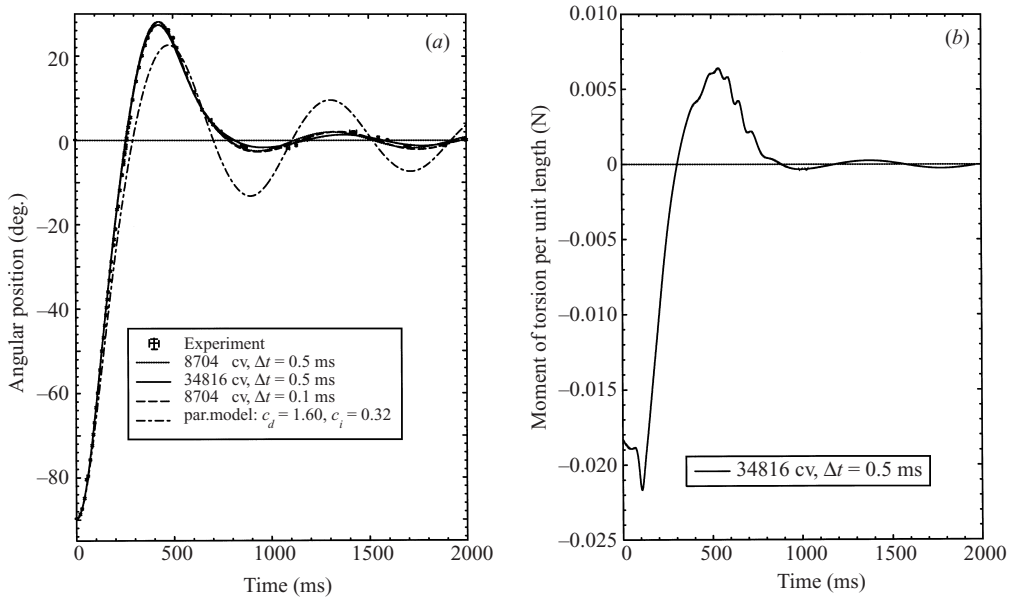


FIGURE 10. Comparison of the computed damping behaviour, the results of the parameter model, and the measurements for −90° initial excursion (*a*). History of the computed fluid moment (*b*).

data almost perfectly, see figure 8(*b*). In fact, the virtual inertia of the fluid $\Theta_F = 1.882 \times 10^{-4}\,\mathrm{rad}^{-1}\,\mathrm{kg\,m}^2$ became larger than that of the structure. From potential theory c_i was derived as 0.25, see Wendel (1950), which would in reality underestimate the effect of virtual inertia. For the higher excursions, however, it was impossible to find constant parameters that provided a sufficiently accurate damping behaviour, see figure 9(*b*) and figure 10(*a*). They could be optimized either for the beginning of the motion or for the following oscillations, but the the accuracy of this model never matched the accuracy of the coupled solution.

Following suggestions from the reviewers, the possibility of reducing the discrepancy between the empirical model and the experimental results by using non-constant parameters was investigated. Elements of the empirical flow model can be traced back to Morison's equation (Morison *et al.* 1950) for the motion of an oscillating cylinder immersed in a fluid of significant inertia. This flow configuration has been studied by, for example, Graham (1980), Bearman *et al.* (1985), Obasaju, Bearman & Graham (1988) and also recently by Dütsch *et al.* (1998). Morison's equation is in turn related to the Basset–Boussinesq–Oseen (BBO) equation for the motion of a solid sphere in a creeping flow. Since the history integral in the BBO equation introduces a flow dependence of the coefficient associated with the acceleration (Θ_F or c_i in equations (3.5) and (3.6)), the empirical model might be improved by including a third parameter to represent the 'fading memory process'. For the present application the kernel of the history integral would have to give a faster decay than that represented by the weighting factor $(t-\tau)^{-1/2}$ of the BBO equation.

For simplicity, the use of a variable drag coefficient $c_d(\varphi)$ and a variable inertia coefficient $c_i(\varphi)$ as functions of the instantaneous amplitude of oscillation φ seemed preferable. Following experimental and analytical results for cylinders in oscillating flow presented by Graham (1980), the appropriate expressions for a lamina were

https://doi.org/10.1017/S0022112002002057 Published online by Cambridge University Press

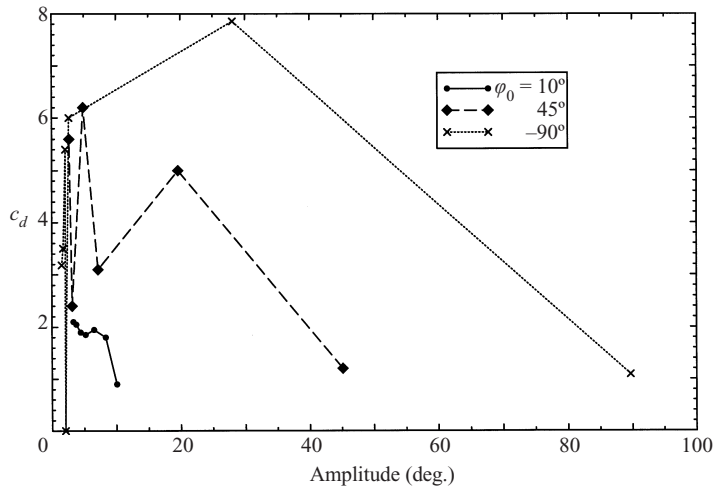


FIGURE 11. Dependence of the coefficient c_d on the oscillation amplitude in the variable coefficients model.

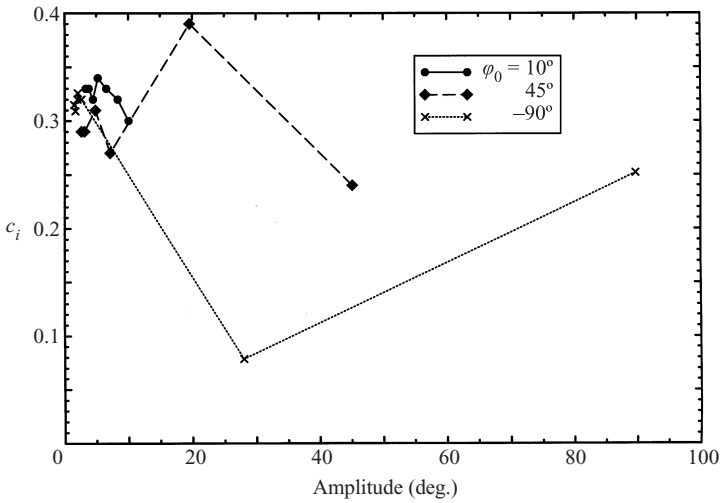


FIGURE 12. Dependence of the coefficient c_i on the oscillation amplitude in the variable coefficients model.

expected to be $c_d = A\varphi^{-1/3}$ and $c_i = B + C\varphi^{2/3}$ (A, B and C constant). This approach was rapidly abandoned, however, because it drastically altered the functional dependence of the drag and inertial terms, so that the corresponding differential equation became highly non-linear and difficult to solve numerically. As an alternative procedure the coefficients c_d and c_i were then assumed to be functions of the starting amplitude (absolute value) for each half-cycle of oscillation of the lamina. The coefficients were held constant during the half-period and were evaluated using the computed damping behaviour from the CFD solution, as given in figures 8(*a*) and 9(*a*) respectively.

Results for c_d shown in figure 11 for all three initial amplitudes φ_0 show a strong dependence on φ. Remarkably, however, in all three cases the damping coefficient for the first half-cycle is about $c_d = 1.0$. The variation of $c_d(\varphi)$ for $\varphi_0 = 10^\circ$ is fairly

https://doi.org/10.1017/S0022112002002057 Published online by Cambridge University Press

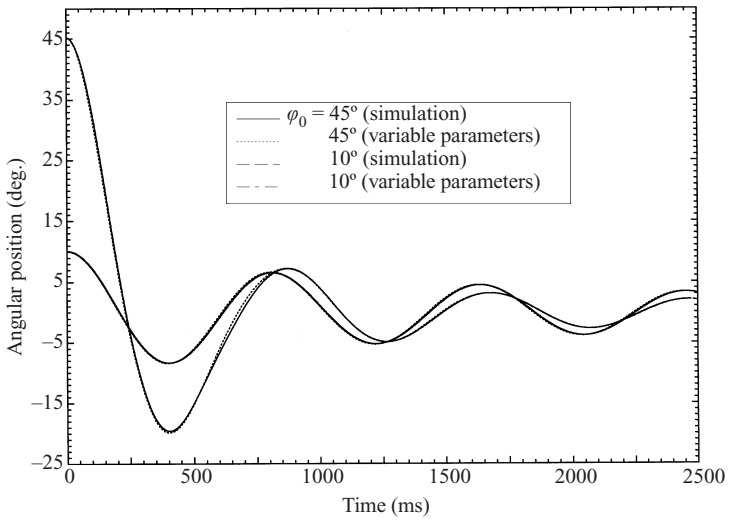


FIGURE 13. Comparison of the damping behaviour with the variable coefficients model and the numerical simulation for 10° and 45°.

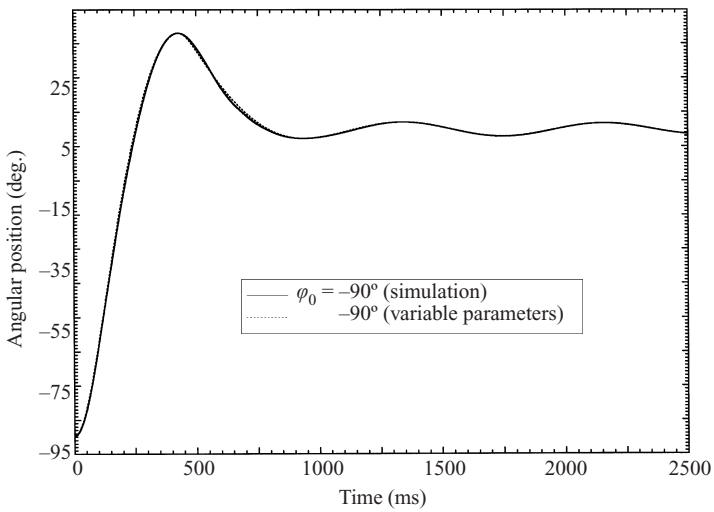


FIGURE 14. Comparison of the damping behaviour with the variable coefficients model and the numerical simulation for −90°.

regular and tends towards $c_d = 2.0$ as $\varphi \to 0$. The variations for $\varphi_0 = 45°$ or $-90°$, on the other hand, are highly irregular. Especially in the range $\varphi < 10°$ the c_d values oscillate widely between 3.0 and 6.0 without an obvious asymptotic limit.

A model using a variable damping coefficient c_d which depends on the initial amplitude φ_0 of each half-oscillation according to the model $c_d = A\varphi_0^n$ thus requires an exponent n which is itself a function of the amplitude. From smoothed curves of $c_d(\varphi)$ it can be deduced that n must increase in magnitude from approximately $-1/3$ at low amplitudes φ to approximately $-3/4$ at large φ. A monotonic reduction of c_d with increasing amplitude φ is obtained for all φ_0 values only over a very restricted range of φ. Even in the range of φ above the onset of oscillations a constant exponent $n = -1/3$ is unsuitable.

https://doi.org/10.1017/S0022112002002057 Published online by Cambridge University Press



FIGURE 15. Vorticity isolines for $\varphi_0 = 10°$ (water).

The investigated model apparently works well with forced oscillations of constant amplitude, but not for damped oscillations for which the initial amplitude must be considered. This is seen indeed quite readily by comparing the curves for $\varphi_0 = 10°, 45°$ and $-90°$ in figures 8 and 9; it is not possible to match the curves for a smaller initial amplitude to part of the curve for a higher initial amplitude. It appears, therefore, that even for the phases of motion with amplitude φ smaller than 10° there is no simple dependence on the amplitude of the preceding half-cycle only. There is an additional dependence on the initial amplitude φ_0 which cannot be represented by the function $c_d = A\varphi^n$.

Applying the same procedure to c_i led to the results in figure 12. The oscillations in c_i are less severe than those in c_d and except at $\varphi = 19.5°$ on the curve for $\varphi_0 = 45°$ and at $\varphi = 27.5°$ for $\varphi_0 = -90°$ all values of c_i lie between 0.24 and 0.34. Although the oscillations decay, even for amplitudes as small as 5° there is no common limiting value for all three cases; the limit appears to lie between 0.29 and 0.33. Because of the small density ratio between solid and liquid, the model c_i = constant is, however, approximately confirmed, consistent with the almost constant values (0.30–0.32) found for c_i in figures 8, 9 and 10. As with c_d a characteristic dependence of c_i on φ cannot

https://doi.org/10.1017/S0022112002002057 Published online by Cambridge University Press



FIGURE 16. Vorticity isolines for $\varphi_0 = 45°$ (water).

be identified. The influence of the initial amplitude is too strong, except perhaps in the asymptotic limit $\varphi \to 0$. The inertial effect of the fluid is adequately represented by a constant added mass. A description of the damping effect through a classical resistance term is, however, insufficient.

Using the coefficients $c_d(\varphi)$ and $c_i(\varphi)$ found in this way for each initial amplitude φ_0, the damped oscillations were recalculated with the parametric model. The curves in figures 13 and 14 show very close agreement with the CFD simulation. This indicates that using $c_d(\varphi_0)$ and $c_i(\varphi_0)$ evaluated at each extremum for the following half-cycle is an adequate approximation. The values of c_d and c_i, however, vary strongly and depend on the initial amplitude φ_0.

4.2.2. *Partitioned solution*

From the partitioned solution the fluid moment acting on the lamina structure was evaluated directly from the pressure and shear stress distributions along the common boundary. The contribution of the shear stresses, however, was almost negligible due to the thinness of the lamina. With respect to the acceleration of the lamina large regions of high or low pressure could be observed either on the front or on the back

https://doi.org/10.1017/S0022112002002057 Published online by Cambridge University Press



FIGURE 17. Vorticity isolines for $\varphi_0 = -90°$ (water).

side of the lamina. The isobars typically showed a butterfly-like formation in the observed cross-section.

From the results of the partitioned computations the fluid and structure dynamics can be described by sets of iso-vorticity lines as presented in figures 15, 16 and 17. For all initial amplitudes the boundary layer separated at the sharp edges of the lamina. One large vortex was created per half-cycle of the oscillation at each tip. Secondary flow structures occurred due to the thickness of the lamina and to the combined effects of interaction with previously shed vortices and the instability of the free shear layers.

Naturally, the spin of a shedding eddy was in the opposite direction to the lamina rotation. This primary effect led to the formation of a pair of counter-rotating vortices during the first cycle of oscillation. This vortex pair moved away quickly from the lamina tip due to its self-induced velocity field and its interaction with the lamina disappeared. In a second step the vorticity dissipated due to the fluid viscosity. However, for the largest amplitude the vortex pair survived right up to the tank walls. This vortex motion could last far beyond the time at which the lamina stopped and, hence, the time delay until repeating the experiment was very important. Recent

https://doi.org/10.1017/S0022112002002057 Published online by Cambridge University Press

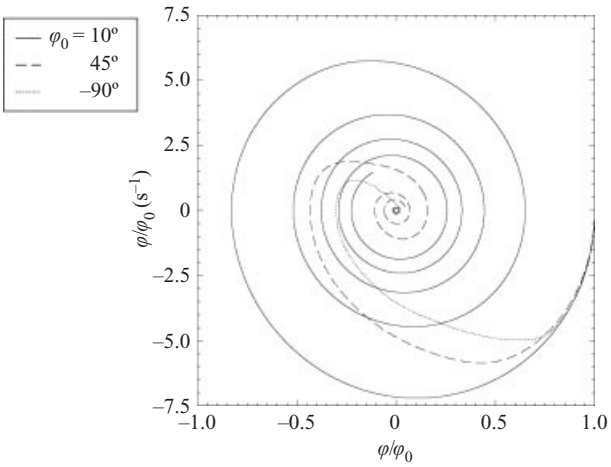


FIGURE 18. Normalized phase diagram from computational data.

investigations by Leweke & Williamson (1998) indicated that such free initially two-dimensional vortex pairs may become unstable. From the good agreement between simulation and experiment, however, there is no indication that the predicted lifetime of the large primary vortex pairs was overestimated.

For the largest initial excursion of $-89.70°$ the vortex dynamics brought the structure almost to rest after just one cycle of oscillation. At the end of the first cycle the lamina had on both sides two strong self-induced eddies close to its front and rear corners. The history of the fluid moment, see figure 10(b), shows that a higher frequency fluctuation arose shortly before the first reversal of the lamina motion. This effect was induced by the instability of the separated boundary layer that formed the second vortex as demonstrated in figure 17. Within the following half-cycle the lamina stopped moving after reaching an intermediate amplitude of 29°. Large computational resources, in particular with respect to the grid resolution, were required in order to predict the time scales and damping of this effect correctly.

Basically, the structure domain transferred a large proportion of its energy into the first vortices, for high initial excursion in particular. The vortices that were shed during the following cycles were, hence, much weaker than the first ones. They kept close to the lamina tip until they dissipated and their influence on the coupled motion was limited. The remaining part of the damping behaviour could be compared to that resulting from small initial excursions. It was also closer to the model assumption as discussed in § 3.4.

In figure 18 the normalized phase diagram is presented as a plot of $\dot{\varphi}/\varphi_0$ versus φ/φ_0. For a linear vibration configuration with constant parameters the curves would coincide, but, except for the very beginning of the motion at $\varphi/\varphi_0 = 1$ the characteristics differ significantly for different initial amplitudes φ_0. The general damping behaviour still depended on the initial excursion, which revealed the strong nonlinearity of the fluid loading. As this was dominated by the transient vortex fields the coupled motion could only be considered correctly by the application of the complete Navier–Stokes equations. The good agreement between the partitioned approach and the experiments supported the assumption that the three-dimensionality of the flow could be neglected for the prediction of the coupled fluid–structure behaviour.

https://doi.org/10.1017/S0022112002002057 Published online by Cambridge University Press

5. Conclusions

The free rotational oscillation of a high-aspect-ratio lamina in a fluid initially at rest was investigated experimentally and computationally. The damped oscillations of the structure were measured for the initial angles of 10°, 45° and −90°. Generally, the structure motion was strongly governed by the nonlinear interaction between the structure and the fluid, which reduced the natural frequencies and increased the damping. In a dense fluid, the motion within the first few cycles of oscillation was largely governed by both the additional inertia due to the fluid and the interaction of the structure with the self-induced vortices. For large initial excursions unexpectedly strong damping effects occurred, which almost stopped the structure motion after the first oscillation.

The predictions of damping of this coupled system by a partitioned numerical analysis of the equations of motion of the structure and the fluid were in close agreement with experimental results. Generally, the flow induced by the symmetric structure remained symmetric for all initial excursions. Computed time sequences of the vorticity field provided an impressive visualization of the flow dynamics, based on pairs of counter-rotating vortices as a fundamental pattern. At increasing amplitudes the structure-related energy was transferred more and more into the shed vortices rather than being dissipated in the boundary layer.

An alternative theory of virtual inertia succeeded only for the range of weak coupling, i.e. at small amplitudes or for a fluid of low density (air). Here, the dynamics of the vortices, which could be considered as the memory of the flow, were less relevant.

This work was sponsored by grants from the Bavarian Consortium for High Performance Computing, FORTWIHR, and from the Volkswagen Foundation. The authors gratefully acknowledge this support.

REFERENCES

Bearman, P. W., Downie, M. J., Graham, J. M. R. & Obasaju, E. D. 1985 Forces on cylinders in viscous oscillatory flow at low Keulegan–Carpenter numbers. *J. Fluid Mech.* **154**, 337–356.

Demirdžić, I. & Perić, M. 1990 Finite volume method for prediction of fluid flow in arbitrarily shaped domains with moving boundaries. *Intl J. Numer. Meth. Fluids* **10**, 771–790.

Durst, F., Perić, M., Schäfer, M. & Schreck, E. 1993 Parallelization of efficient numerical methods for flows in complex geometries. In *Flow Simulation with High-Performance Computers I* (ed. E. H. Hirschel). Notes on Numerical Fluid Mechanics vol. 38, pp. 79–92. Vieweg.

Dütsch, H., Durst, F., Becker, S. & Lienhart, H. 1998 Low-Reynolds-number flow around an oscillating circular cylinder at low Keulegan–Carpenter numbers. *J. Fluid Mech.* **360**, 249–271.

Dütsch, H., Melling, A. & Durst, F. 1999 Fluid damped oscillations of a lamina at large initial amplitudes. In *High Performance Scientific and Engineering Computing* (ed. H.-J. Bungartz, F. Durst & C. Zenger). Lecture Notes in Computational Science and Engineering, vol. 8. Springer.

Graham, J. M. R. 1980 The forces on sharp-edged cylinders in oscillatory flow at low Keulegan–Carpenter numbers. *J. Fluid Mech.* **97**, 331–346.

Horsten, J., van Steenhoven, A. & van Campen, D. 1990 A fluid–structure interaction model for heart valves with a single degree of freedom. In *Proc. Eight GAMM-Conf. on Numerical Methods in Fluid Mechanics* (ed. P. Wesseling). Notes on Numerical Fluid Mechanics, vol. 29, p. 201 ff. Vieweg.

Kerh, T. J. J. L. & Wellford, L. C. 1997 Transient fluid–structure interaction in a control valve. *Trans. ASME J. Fluids Engng* **119**, 354–359.

Leweke, T. & Williamson, C. H. K. 1998 Large-scale instability and small-scale transition in vortex pairs. *Institut de Recherche sur les Phénomènes Hors Equilibre Rep.*

https://doi.org/10.1017/S0022112002002057 Published online by Cambridge University Press

Lin, X. W., Bearman, P. W. & Graham, J. M. R. 1996 A numerical study of oscillatory flow about a circular cylinder for low values of beta parameter. *J. Fluids Struct*. **10**, 501–526.

Morison, J. R., O'Brien, M. P., Johnson, J. W. & Schaaf, S. A. 1950 The force exerted by surface waves on piles. *Petrol. Trans. AIME* **189**, 149–154.

Obasaju, E. D., Bearman, P. W. & Graham, J. M. R. 1988 A study of forces, circulation and vortex patterns around a circular cylinder in oscillating flow. *J. Fluid Mech.* **196**, 467–494.

Patankar, S. V. 1980 *Numerical Heat Transfer and Fluid Flow*. Hemisphere.

Wendel, K. 1950 Hydrodynamische Massen und hydrodynamische Massenträgheitsmomente. In *Jahrbuch der Schiffbautechnischen Gesellschaft*, vol. 44, pp. 207–255. Springer.

https://doi.org/10.1017/S0022112002002057 Published online by Cambridge University Press